Riemann-Encircling Exceptional Points for Efficient Asymmetric Polarization-Locked Devices

Aodong Li, Weijin Chen, Heng Wei, Guowei Lu, Andrea Alù, Cheng-Wei Qiu, and Lin Chen

Phys. Rev. Lett. **129**, 127401 — Published 13 September 2022

DOI: 10.1103/PhysRevLett.129.127401

Riemann-encircling exceptional points for efficient asymmetric polarization-locked devices

Aodong Li[1,†], Weijin Chen[2,†], Heng Wei[2], Guowei Lu[3], Andrea Alù[4,5], Cheng-Wei Qiu[2] and Lin Chen[1,3,*]

[1] Wuhan National Laboratory for Optoelectronics and School of Optical and Electronic Information, Huazhong University of Science and Technology, Wuhan 430074, China

[2] Department of Electrical and Computer Engineering, National University of Singapore, Singapore 117583, Singapore

[3] State Key Laboratory for Mesoscopic Physics, School of Physics, Peking University, Beijing 100871, China

[4] Photonics Initiative, Advanced Science Research Center, City University of New York, New York, NY 10031, USA

[5] Physics Program, Graduate Center, City University of New York, New York, NY 10016, USA

* Corresponding author.

† These authors contributed equally to this work.

Abstract

Dynamically encircling exceptional points (EPs) has unveiled intriguing chiral dynamics in photonics. However, the traditional approach based on an open manifold of Hamiltonian parameter space fails to explore trajectories that pass through an infinite boundary. Here, by mapping the full parameter space onto a closed manifold of the Riemann sphere, we introduce a framework to describe encircling-EP loops. We demonstrate that an encircling trajectory crossing the north vertex can realize near-unity asymmetric transmission. An efficient gain-free, broadband asymmetric polarization-locked device is realized by mapping the encircling path onto L-shaped silicon waveguides.

In a non-Hermitian system obeying parity-time (PT) symmetry, two or more eigenvalues and eigenstates are simultaneously degenerate at exceptional points (EPs). A variety of intriguing phenomena, such as sensing enhancement [1-3], unidirectional invisibility [4,5], topological light control [6,7] and asymmetric mode conversion [8-15] have been demonstrated at these singularities, closely linked to their topological features, and they have attracted a growing interest in optics [1,7,8,16-26], acoustics [27-29], thermodynamics [30], electronics [31,32] and quantum mechanics [33].

When a Hamiltonian adiabatically encircles an EP twice, the Berry phase is π, indicating a self-intersecting Riemann surface (Rsurf) around the EP [34]. Recent studies have demonstrated that this feature enables a chiral response: by dynamically encircling an EP in clockwise (CW) or anticlockwise (ACW) direction leads to different final states, regardless of the starting states. Such chiral response has been demonstrated by mapping the required Hamiltonian parameters onto PT symmetric arrangements of waveguides [8,20,35]. Most previous studies have been applying this feature to realize asymmetric conversion of modes in optical waveguides, but they failed to achieve high transmission efficiencies due to path-dependent loss [8,12,13,20,36,37]. The reason is that the traditional approach to EP encircling is based on an open manifold in the Hamiltonian parameter space. Such approach neglects a set of loops passing through the infinite boundary, enabling low path-dependent losses. Due to significant challenges in practical experimental implementations, high-efficiency polarization-locked device has not been achieved to date [10,38].

In this Letter, we demonstrate that the full Hamiltonian parameter space can be mapped onto the Riemann sphere (Rsph), over which infinite points lying on its boundary are associated with the same eigenstates, and converge to the north vertex. Benefitting from the Rsph mapping, we can encircle an EP along a continuous and closed trajectory passing through the north vertex and achieve highly-efficient

asymmetric transmission. We present experimental results mapping this trajectory onto L-shaped waveguides, demonstrating near-unity asymmetric conversion efficiency at 1550 nm. Such a functionality corresponds to an asymmetric polarization-locked device (APLD), since the output polarization state is locked irrespective of the input polarization states [39].

A system state $|\psi\rangle$ propagating along z follows a Schrödinger-type equation $i\partial/\partial z|\psi\rangle = H|\psi\rangle$, with second-order Hamiltonian

$$H = \begin{bmatrix} \beta & \kappa \\ \kappa & -\beta - i\gamma \end{bmatrix} \quad (1)$$

where β, γ and κ represent the detuning, relative gain/loss rate and coupling strength of the system, respectively. The two eigenvalues are $E_{1,2} = -i\gamma/2 \pm \sqrt{\kappa^2 + (\beta + i\gamma/2)^2}$, and the associated eigenstates are $|\psi_{1,2}\rangle = \left[\sqrt{1 \pm K}, \pm\sqrt{1-(\pm K)}\right]^T / \sqrt{2}$, with $K = (\beta + i\gamma/2)/\sqrt{\kappa^2 + (\beta + i\gamma/2)^2}$. In the two-dimensional (2-D) parameter space $\zeta = (\beta/\kappa, \gamma/\kappa)$, the EPs are located at $\zeta = (0, 2)$ and $\zeta = (0, -2)$. When H approaches the points at infinity in ζ, i.e., $\beta/\kappa \to \pm\infty$ and/or $\gamma/\kappa \to \pm\infty$, the two eigenstates converge to $|\psi_1\rangle = [1, 0]^T$ and $|\psi_2\rangle = [0, 1]^T$, corresponding to E_1 and E_2 [$|\mathrm{Im}(E_1)| \le |\mathrm{Im}(E_2)|$], respectively. The energy spectra form a self-intersecting Rsurf in ζ, and the topological features can be expressed as a Berry phase $\Phi = \pi$ when an EP is encircled twice with a quasi-dynamic approach [40]. The Berry phase around a path **C** can be defined as $\Phi = i\int_{\mathbf{C}} \langle\chi(\zeta)|\nabla_\zeta \psi(\zeta)\rangle \cdot d\zeta$, where $\langle\chi(\zeta)|$ is the left eigenstate and $\langle\chi(\zeta)|H = \langle\chi(\zeta)|E$, i.e., $H^\dagger|\chi(\zeta)\rangle = E^*|\chi(\zeta)\rangle$ [41-43]. Since H is a symmetric Hamiltonian according to Eq. (1), i.e., $H^T = H$, we have $H^\dagger = H^*$ and $|\chi(\zeta)\rangle = |\psi^*(\zeta)\rangle$. If the Hamiltonian evolves along the parameter space boundary [Fig. 1(a)], $\psi(\zeta)$ is constant, i.e., $|\nabla_\zeta \psi(\zeta)\rangle = 0$, which makes Φ equal to zero.

To present the trajectory induced by the infinite boundary, we can represent the full parameter space over a Rsph of radius 2, as schematically shown in Fig. 1(b). The mapping procedure, called stereographic projection, is based on the following steps: first, the center of the sphere is aligned with the origin of the 2-D parameter space as denoted in Fig. 1(a); then, the north pole (blue point on Rsph) is connected to the yellow point in the 2-D parameter space (gray plane) to form a line; last, its intersecting point with the Rsph is the mapping point (black point). Here, we provide some examples to show connections between loops and its mapping counterparts. When the loop only encircles the origin of the parameter space, the mapping loop is in the southern hemisphere [Fig. 1(c)]; when the loop expands to include two EPs, the mapping loop is in the northern hemisphere [Fig. 1(d)]; and when the loop continues to expand and becomes the infinite boundary (blue dashed line), the mapping loop converges to the north vertex (blue point) [Fig. 1(b)]. The mapping operation can also be analytically expressed: we assume that the Rsph radius is 2, and the mapping relation from the 2-D parameter space to the Rsph is $\beta/\kappa = 2\cot(\varphi_1/2)\cos(\varphi_2)$ and $\gamma/\kappa = 2\cot(\varphi_1/2)\sin(\varphi_2)$, where φ_1 is the polar angle and φ_2 is the azimuthal angle as denoted in Fig. 1(b). Since all the points on the parameter space boundaries with generally different loss rates are mapped onto the north vertex, the associated loss rate can be an arbitrary value (Supplementary Material [44], Note 1).

As a function of their Berry phase, encircling loops can be divided into two groups, characterized by $\Phi = 0$ and π. Encircling two EPs, as well as no EP, results in a Berry phase $\Phi = 0$. Therefore, the north vertex does not contribute to the Berry phase. In both cases, Rsph is split by the loop into two surfaces, one containing two EPs and the other containing no EPs [Figs. 1(c) and 1(d)]. In contrast, encircling trajectories including one EP splits the Rsph into two surfaces, each containing one EP [Figs. 1(e) and 1(f)] associated with a Berry phase $\Phi = \pi$. The former one in Fig. 1(e) does not pass through the infinite boundary, and therefore the trajectories on both Rsph and real parameter space are closed. In the case of the latter one in Fig. 1(f),

since the trajectory in real parameter space is blocked by the infinite boundary (dashed blue line), it is open. By mapping the infinite boundary with the same eigenstates onto the north vertex, we can achieve a closed mapping trajectory (black solid line) on the Rsph. In this way, both mapping trajectories in Figs. 1(e) and 1(f) show their topological equivalence, since the closed loops encircle each one of the two EPs. On the Rsph, it is not necessary to distinguish which EP is encircled, since the loop that encircles one EP shares the same Berry phase with the loop that encircles the other EP, i.e., they are topologically equivalent (Supplementary Material [44], Note 2).

The transmission loss accumulated along the mapping trajectory can be also interpreted from the perspective of Rsph: the mapping trajectories in Figs. 1(e) and 1(f) encircle each of the two EPs simultaneously, and the distance relative to each EP located in the gain or loss region determines the transmission loss. The conventional mapping trajectory in Fig. 1(e) is close to the loss EP [$\zeta = (0, 2)$], associated with path-dependent loss along the entire path ($\gamma/\kappa > 0$), making the system prone to low transmittance. The loss difference between the two eigenstates causes the occurrence of nonadiabatic transitions (NATs), leading to an asymmetric response [11,12,45]. Instead, the mapping trajectory in Fig. 1(f), located in the middle of the two EPs, is not associated with any loss except at the north vertex, and hence it enables high-efficiency transmission. In Fig. 1(f), the NAT process is guaranteed by introducing a non-zero loss rate at the north vertex and exerting a sufficiently long evolution time to dissipate $|\psi_2\rangle$. See Supplementary Material [44], Note 3 for the evolution dynamics on how the loss affects the final output states. Meanwhile, through the mapping of Rsph we ensure that this loop indeed encircles each EP, leading to an asymmetric response. Thus, we simultaneously achieve both high efficiency and largely asymmetric transmission following this trajectory.

This specific trajectory can be mapped onto a suitably designed silicon waveguide tailored for APLD, as schematically depicted in Fig. 2(a). The right

waveguide supports two orthogonal eigenmodes with different polarization directions, i.e., R1 ($|\psi_1\rangle$) and R2 ($|\psi_2\rangle$) modes with effective refractive indices n_{R1} and n_{R2} ($n_{R1} < n_{R2}$), respectively. θ represents the angle between the polarization direction of R1 and the $+45°$ axis [Fig. 2(b)]. In this configuration, the eigenmode in the right waveguide can be expressed as $|\psi\rangle = [A_1, A_2]^T$, in which A_1 and A_2 indicate the projection components of the normalized electric field amplitude along $+45°$ and $-45°$, respectively. Consequently, the Hamiltonian parameters in Eq. 1 can be expressed as $\beta = k_0(n_{R1} - n_{R2})(\sin^2\theta - \cos^2\theta)/2$, $\kappa = k_0(n_{R1} - n_{R2})\sin\theta\cos\theta$. γ is the loss rate exerted on the components of the electric field along $-45°$, and $k_0 = 2\pi/\lambda$ is the wavenumber, with λ being the wavelength (Supplementary Material [44], Note 4).

At the starting point A, the R1 mode is transverse-magnetic (TM) polarized with $\theta = 45°$, corresponding to $\beta/\kappa = 0$ [Fig. 2(c)]. Between A and B, θ changes monotonously from $45°$ to $0°$, reducing β/κ from 0 to $-\infty$, associated with the evolution path from A to B along the longitude on the Rsph [illustration of Fig. 2(a)]. Between B and C, the right waveguide is axisymmetric along $+45°$ axis, so that R1 is polarized along $+45°$ direction with $\theta = 0°$, resulting in $\kappa = 0$ and $\beta/\kappa = \infty$ [Fig. 2(c)]. The left waveguide between B and C is designed to absorb the eigenmode polarized along $-45°$ direction in the right waveguide via adiabatic coupling, associated with $\gamma > 0$. The whole evolution path between B and C takes place at the north vertex on the Rsph. Between C and D, β/κ is varied monotonously from $+\infty$ to 0 as θ is reduced from $0°$ to $-45°$, and the Hamiltonian evolves from C to D along the longitude on the Rsph. Although β, γ, and κ are finite, the Hamiltonian parameter space boundary is accessible based on the specifically tailored L-shaped waveguide.

Figures 3(a-d) show the evolution trajectory of the system state on Rsurf (not Rsph, mapped here with $\mathrm{atan}(E)/\kappa$ in the third dimension to cast it into a finite plot) for CW and ACW loops around the EP, where the CW and ACW loops correspond to light propagating along $+z$ and $-z$ in the right waveguide, respectively. The difference of the two eigenvalues is minimum at the EP, but both drastically change close to the EP [46]. In contrast, the difference of the two eigenvalues is maximum, but both tend to converge when approaching the infinity point. For the CW loop with $[1,1]^T$ input, associated with the TE mode, $[1,1]^T$ evolves to $[0,1]^T$ when the Hamiltonian varies slowly from A to B [Fig. 3(a)]. Meanwhile, $[1,0]^T$ is excited at B, due to the fact that rigorous adiabaticity cannot be fully guaranteed. During the NAT process from B to C, $[0,1]^T$ is dissipated and $[1,0]^T$ is preserved, making the dominant eigenstate of the system switch from $[0,1]^T$ to $[1,0]^T$. Finally, the Hamiltonian returns to the destination D with $[1,1]^T$, and the corresponding output mode is TE. For the CW loop with $[1,-1]^T$ input [Fig. 3(b)], associated with the TM mode, the dominant eigenstate during the evolution is always lossless because a NAT does not occur, and the final output state is $[1,1]^T$, TE in nature. This indicates that the output mode for the CW direction is locked to TE, irrespective of the input mode. For the ACW loop [Figs. 3(c, d)], the output state is locked to $[1,-1]^T$, associated with TM polarization. The two sheets of Rsurf are self-intersecting, and the adiabatic evolution path between B and C is vertical, as the slope at B and C is infinite on this choice of Rsurf. A NAT occurs between B and C in Figs. 3(a, d), during which the evolution path switches from the blue to the red branch.

The L-shaped silicon waveguides shown in Fig. 2(a) are carefully tailored to map this evolution path by establishing the relation between structural parameters and the Hamiltonian parameters (Supplementary Material [44], Note 5). For the CW (ACW)

loop with TE (TM) mode input to the right waveguide at A (D), the TE (TM) mode evolves to R2 polarized along $-45°$ at B (C) [Fig. 4(a)]. Meanwhile, R1 polarized along $+45°$ is excited because the length between A and B (D and C) is limited and the adiabatic evolution is not strictly satisfied. The device length between B and C is long enough so that R2 is fully absorbed by the left waveguide and the triggered R1 mode is retained, i.e., a NAT occurs. Finally, R1 evolves to TE (TM) from C to D (B to A) with a relatively low field intensity. For the CW (ACW) loop with TM (TE) input to the right waveguide at A (D), it evolves to R1 mode at B (C). The triggered R2 mode is absorbed between B and C, and R1 mode eventually evolves to TE (TM) mode from C to D (B to A).

Figure 4(b) show the fabricated devices, with grating couplers (GCs), polarization beam splitter and rotators (PBRs) for measurement. The measured transmission efficiencies for TE and TM mode input are shown in Fig. 4(c) and 4(d), respectively (see Supplementary Material [44], Notes 6, 7 for the fabrication details and measurement scheme). $T_{P\to Q}$ ($T_{P\leftarrow Q}$) represents the transmission efficiency of Q mode from the output port for input P mode from the left (right) port (P or Q mode refer to TE or TM mode). For a left-side input, $T_{TE\to TE} >> T_{TE\to TM}$ and $T_{TM\to TE} >> T_{TM\to TM}$, indicating that the output mode is locked to TE. For right-side excitation, $T_{TM\leftarrow TE} >> T_{TE\leftarrow TE}$ and $T_{TM\leftarrow TM} >> T_{TE\leftarrow TM}$, indicating that the output mode is locked to TM. It can be observed that $T_{TM\to TE}$ and $T_{TM\leftarrow TE}$ are close to 100% around 1550 nm. The mode crosstalk is defined as the energy ratio of the undesired mode to total output [47]. The mode crosstalks $\mathrm{TM}\to\mathrm{TE}$, $\mathrm{TM}\leftarrow\mathrm{TE}$, and $\mathrm{TE}\to\mathrm{TE}$ are all below -20 dB, while $\mathrm{TM}\leftarrow\mathrm{TM}$ is below -10 dB. The experimental results well validate the asymmetric polarization-locked performance. It should be noted that the APLD is sensitive to the alignment error, and therefore the alignment should be carefully controlled in fabrication (Supplementary Material [44], Note 8).

Here, we can also treat the APLD as a 3-section optical system (Supplementary

Material [44], Note 9). The AB/CD section is used as a leaky polarization controller that converts the input mode into the dominant eigenmode and its orthogonal eigenmode. The BC section serves as a selective optical attenuator that takes away one of the eigenmodes. The approach of using a 3-section optical system can also be extended to develop asymmetrical polarization conversion devices for spatial light [48]. These alternative schemes however are limited in terms of operational bandwidth. EP encircling on the contrary ensures large working bandwidths, due to adiabatic parameter evolution of the energy spectra [8,15,20]. Our simulations predict that the practical bandwidth of the described operation can be as large as the entire range 1450-1750 nm (Supplementary Material [44], Note 10). The presented Riemann-encircling strategy can be extended to study asymmetrical state-locked response in a multi-state non-Hermitian system (Supplementary Material [44], Note 11].

In conclusion, we have shown that dynamically encircling an EP on Rsph can enable asymmetric polarization conversion, and a continuous encircling trajectory passing through the north vertex can realize near-unity asymmetric transmission. We experimentally demonstrated nearly 100% asymmetric polarization conversion between TE and TM modes with mode crosstalk below −20 dB at 1550 nm in silicon waveguides. These results enable the practical realization of highly efficient gain-free, broadband asymmetric polarization conversion on-chip, and hold the promise for new opportunities for optical devices and applications.

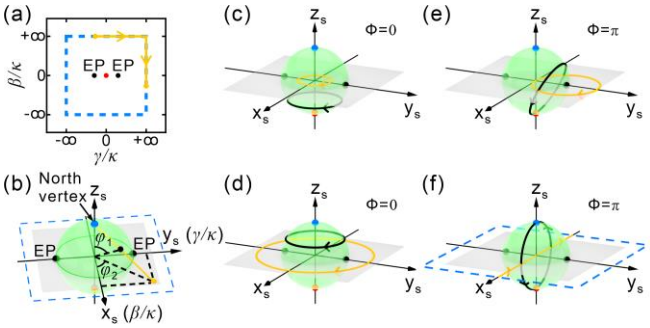

239

240 **FIG. 1.** (a) Hamiltonian parameter space described by $\zeta = (\beta/\kappa, \gamma/\kappa)$. The yellow line shows an

241 evolution path along the parameter space boundary (blue dashed line). (b) Rsph

242 ($x_s^2 + y_s^2 + z_s^2 = 2^2$, $x_s = 2\sin\varphi_1\cos\varphi_2$, $y_s = 2\sin\varphi_1\sin\varphi_2$ and $z_s = 2\cos\varphi_1$) describing the

243 Hamiltonian parameter space. (c-f) The evolution loops on Rsph (black curves) and in the 2-D

244 parameter space (yellow curves) when encircling (c) no EP, (d) two EPs, and (e), (f) one EP. The

245 loop in (f) locates in the center of the two EPs.

246

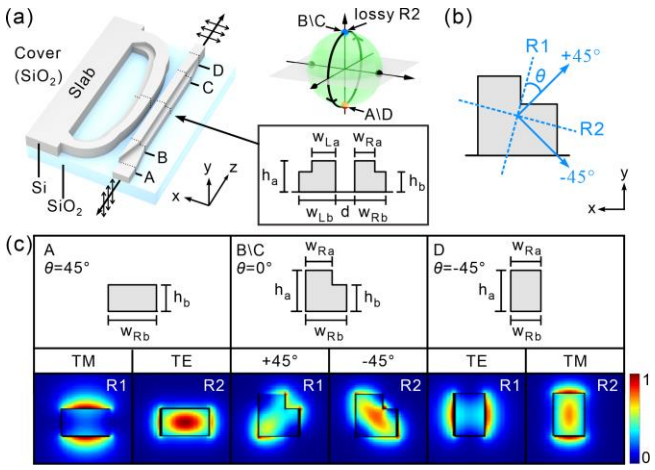

247

248 **FIG. 2.** (a) APLD made of silicon waveguides. The full height of the L-shaped waveguide is
249 $h_a = 340\,\text{nm}$, and the height of the lower waveguide is $h_b = 220\,\text{nm}$. The width of the upper
250 waveguide and the full waveguide is w_{La} (w_{Ra}) and w_{Lb} (w_{Rb}) for the left (right) waveguide,
251 respectively. The gap separation between the two waveguides is d. (b) The polarization
252 directions for R1 and R2 modes. (c) The cross sections of the right waveguide at A, B\C, and D,
253 and their associated electric field intensity distributions for the R1 and R2 eigenmodes.

254

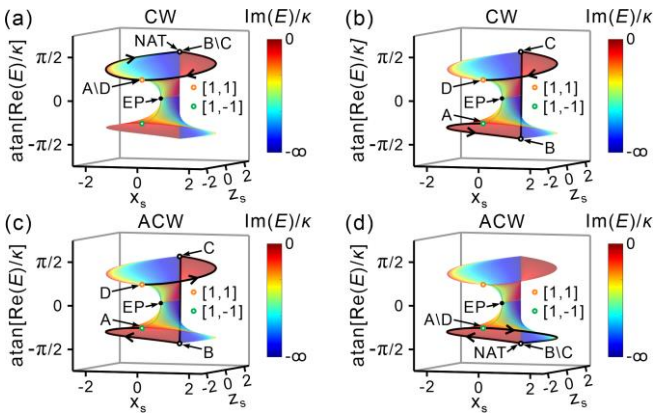

255

256 **FIG. 3.** (a),(b) CW loops on Rsurf formed by the real part of the eigenvalues of H when the input

257 state is (a) $[1,1]^T$ and (b) $[1,-1]^T$. The Rsurf is extracted by casting the hemisphere with $y_s \geq 0$

258 (pure lossy case) of the Rsph onto the x_s-z_s plane. The color of the surface indicates the imaginary

259 part of the eigenvalues of H, in which a smaller imaginary part indicates a larger loss. (c), (d)

260 ACW loops when the input state is (c) $[1,1]^T$ and (d) $[1,-1]^T$.

261

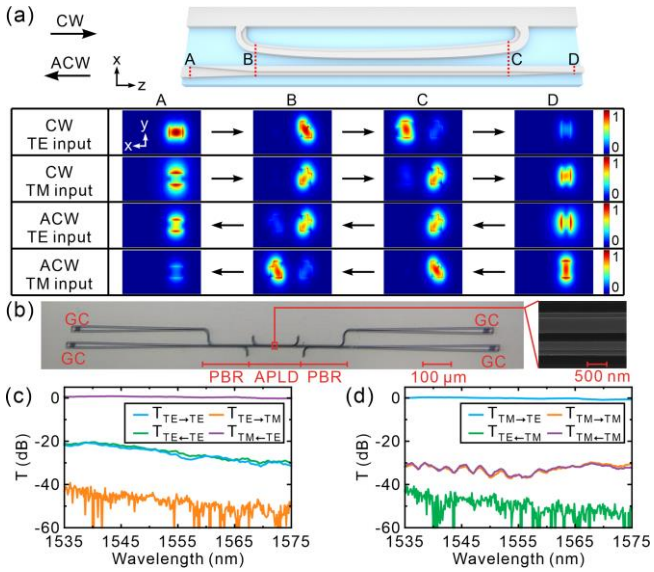

FIG. 4. (a) The cross-sectional electric field intensity distributions at A, B, C, and D. (b) Optical microscope images of the fabricated APLD, where the L-shaped waveguides are partially depicted by the SEM image on the right panel. (c), (d) Measured transmittance spectra over 1535-1575 nm wavelength range as (c) TE and (d) TM modes are injected, respectively.

References

[1] H. Hodaei, A.U. Hassan, S. Wittek, H. Garcia-Gracia, R. El-Ganainy, D.N. Christodoulides, M. Khajavikhan, Nature **548**, 187-191 (2017).

[2] W. Chen, S. Kaya Ozdemir, G. Zhao, J. Wiersig, L. Yang, Nature **548**, 192-196 (2017).

[3] J.-H. Park, A. Ndao, W. Cai, L. Hsu, A. Kodigala, T. Lepetit, Y.-H. Lo, B. Kanté, Nat. Phys. **16**, 462-468 (2020).

[4] Z. Lin, H. Ramezani, T. Eichelkraut, T. Kottos, H. Cao, D.N. Christodoulides, Phys. Rev. Lett. **106**, 213901 (2011).

[5] L. Feng, Y.L. Xu, W.S. Fegadolli, M.H. Lu, J.E. Oliveira, V.R. Almeida, Y.F. Chen, A. Scherer, Nat. Mater. **12**, 108-113 (2013).

[6] H. Zhao, X. Qiao, T. Wu, B. Midya, S. Longhi, L. Feng, Science **365**, 1163-1166 (2019).

[7] W. Song, W. Sun, C. Chen, Q. Song, S. Xiao, S. Zhu, T. Li, Phys. Rev. Lett. **123**, 165701 (2019).

[8] J. Doppler, A.A. Mailybaev, J. Bohm, U. Kuhl, A. Girschik, F. Libisch, T.J. Milburn, P. Rabl, N. Moiseyev, S. Rotter, Nature **537**, 76-79 (2016).

[9] S.N. Ghosh, Y.D. Chong, Sci. Rep. **6**, 19837 (2016).

[10] A.U. Hassan, B. Zhen, M. Soljacic, M. Khajavikhan, D.N. Christodoulides, Phys. Rev. Lett. **118**, 093002 (2017).

[11] X.-L. Zhang, T. Jiang, C.T. Chan, Light Sci. Appl. **8**, 88 (2019).

[12] X.-L. Zhang, S. Wang, B. Hou, C.T. Chan, Phys. Rev. X **8**, 021066 (2018).

[13] X.-L. Zhang, C.T. Chan, Commun. Phys. **2**, 63 (2019).

[14] Q. Liu, S. Li, B. Wang, S. Ke, C. Qin, K. Wang, W. Liu, D. Gao, P. Berini, P. Lu, Phys. Rev. Lett. **124**, 153903 (2020).

[15] A. Li, J. Dong, J. Wang, Z. Cheng, J.S. Ho, D. Zhang, J. Wen, X.-L. Zhang, C.T. Chan, A. Alù, C.-W. Qiu, L. Chen, Phys. Rev. Lett. **125**, 187403 (2020).

[16] A. Guo, G.J. Salamo, D. Duchesne, R. Morandotti, M. Volatier-Ravat, V. Aimez, G.A. Siviloglou, D.N. Christodoulides, Phys. Rev. Lett. **103**, 093902 (2009).

[17] M. Lawrence, N. Xu, X. Zhang, L. Cong, J. Han, W. Zhang, S. Zhang, Phys. Rev. Lett. **113**, 093901 (2014).

[18] B. Peng, Ş.K. Özdemir, M. Liertzer, W. Chen, J. Kramer, H. Yılmaz, J. Wiersig, S. Rotter, L. Yang, Proc. Natl. Acad. Sci. **113**, 6845-6850 (2016).

[19] L. Feng, R. El-Ganainy, L. Ge, Nat. Photon. **11**, 752-762 (2017).

[20] J.W. Yoon, Y. Choi, C. Hahn, G. Kim, S.H. Song, K.Y. Yang, J.Y. Lee, Y. Kim, C.S. Lee, J.K. Shin, H.S. Lee, P. Berini, Nature **562**, 86-90 (2018).

[21] M.P. Hokmabadi, A. Schumer, D.N. Christodoulides, M. Khajavikhan, Nature **576**, 70-74 (2019).

[22] Y.-H. Lai, Y.-K. Lu, M.-G. Suh, Z. Yuan, K. Vahala, Nature **576**, 65-69 (2019).

[23] M.-A. Miri, A. Alù, Science **363**, eaar7709 (2019).

[24] A.L.M. Muniz, M. Wimmer, A. Bisianov, U. Peschel, R. Morandotti, P.S. Jung, D.N. Christodoulides, Phys. Rev. Lett. **123**, 253903 (2019).

[25] S. Xia, D. Kaltsas, D. Song, I. Komis, J. Xu, A. Szameit, H. Buljan, K.G. Makris, Z. Chen, Science **372**, 72-76 (2021).
[26] Z. Chen, M. Segev, eLight **1**, 2 (2021).
[27] K. Ding, G. Ma, Z.Q. Zhang, C.T. Chan, Phys. Rev. Lett. **121**, 085702 (2018).
[28] W. Tang, X. Jiang, K. Ding, Y.-X. Xiao, Z.-Q. Zhang, C.T. Chan, G. Ma, Science **370**, 1077-1080 (2020).
[29] H.-Z. Chen, T. Liu, H.-Y. Luan, R.-J. Liu, X.-Y. Wang, X.-F. Zhu, Y.-B. Li, Z.-M. Gu, S.-J. Liang, H. Gao, L. Lu, L. Ge, S. Zhang, J. Zhu, R.-M. Ma, Nat. Phys. **16**, 571-578 (2020).
[30] Y. Li, Y.-G. Peng, L. Han, M.-A. Miri, W. Li, M. Xiao, X.-F. Zhu, J. Zhao, A. Alù, S. Fan, C.-W. Qiu, Science **364**, 170-173 (2019).
[31] Z. Dong, Z. Li, F. Yang, C.-W. Qiu, J.S. Ho, Nat. Electron. **2**, 335-342 (2019).
[32] L. Shao, W. Mao, S. Maity, N. Sinclair, Y. Hu, L. Yang, M. Lončar, Nat. Electron. **3**, 267-272 (2020).
[33] F. Klauck, L. Teuber, M. Ornigotti, M. Heinrich, S. Scheel, A. Szameit, Nat. Photon. **13**, 883-887 (2019).
[34] C. Dembowski, B. Dietz, H.D. Gräf, H.L. Harney, A. Heine, W.D. Heiss, A. Richter, Phys. Rev. E **69**, 056216 (2004).
[35] F. Yu, X.-L. Zhang, Z.-N. Tian, Q.-D. Chen, H.-B. Sun, Phys. Rev. Lett. **127**, 253901 (2021).
[36] Y. Choi, C. Hahn, J.W. Yoon, S.H. Song, P. Berini, Nat. Commun. **8**, 14154 (2017).
[37] X.-L. Zhang, J.-F. Song, C.T. Chan, H.-B. Sun, Phys. Rev. A **99**, 063831 (2019).
[38] G. Lopez-Galmiche, H.E. Lopez Aviles, A.U. Hassan, A. Schumer, T. Kottos, P.L. LiKamWa, M. Khajavikhan, D.N. Christodoulides, Omnipolarizer Action via Encirclement of Exceptional Points, Conference on Lasers and Electro-Optics, Optical Society of America, Washington, DC, 2020, pp. FM1A.3.
[39] S.S. Aleshkina, A. Fedotov, D. Korobko, D. Stoliarov, D.S. Lipatov, V.V. Velmiskin, V.L. Temyanko, L.V. Kotov, R. Gumenyuk, M.E. Likhachev, Opt. Lett. **45**, 2275-2278 (2020).
[40] T. Gao, E. Estrecho, K.Y. Bliokh, T.C.H. Liew, M.D. Fraser, S. Brodbeck, M. Kamp, C. Schneider, S. Höfling, Y. Yamamoto, F. Nori, Y.S. Kivshar, A.G. Truscott, R.G. Dall, E.A. Ostrovskaya, Nature **526**, 554-558 (2015).
[41] M.V. Berry, Proceedings of the Royal Society of London. A. Mathematical and Physical Sciences **392**, 45-57 (1984).
[42] F. Keck, H.J. Korsch, S. Mossmann, Journal of Physics A: Mathematical and General **36**, 2125-2137 (2003).
[43] S.-D. Liang, G.-Y. Huang, Phys. Rev. A **87**, 012118 (2013).
[44] See Supplementary Material for more details on imaginary part of the eigenvalues, evolution dynamics with different losses, Schrödinger-type equation for the L-shaped waveguide, structural paramters, fabrication process, measurement scheme, alignment error analysis, asymmetric polarization conversion, simulation

results, and asymmetric state-locked response in an N-state system.
[45] A.U. Hassan, G.L. Galmiche, G. Harari, P. LiKamWa, M. Khajavikhan, M. Segev, D.N. Christodoulides, Phys. Rev. A **96**, 052129 (2017).
[46] A. Lupu, V.V. Konotop, H. Benisty, Sci. Rep. **7**, 13299 (2017).
[47] L.-W. Luo, N. Ophir, C.P. Chen, L.H. Gabrielli, C.B. Poitras, K. Bergmen, M. Lipson, Nat. Commun. **5**, 3069 (2014).
[48] J.B. Khurgin, Y. Sebbag, E. Edrei, R. Zektzer, K. Shastri, U. Levy, F. Monticone, Optica **8**, 563-569 (2021).

Acknowledgement This work has been supported by National Natural Science Foundation of China (Grant Nos. 11674118, 12074137), State Key Laboratory of Artificial Microstructure & Mesoscopic Physics (Peking University), State Key Laboratory of Advanced Technology for Materials Synthesis and Processing (Wuhan University of Technology), Air Force Office of Scientific Research MURI program, and the Simons Foundation. We thank Pan Li in the Center of Micro-Fabrication and Characterization (CMFC) of WNLO for the support in plasma enhanced chemical vapor deposition, and the Center for Nanoscale Characterization & Devices (CNCD), WNLO, HUST for the support in SEM measurement.

Competing interests The authors declare that they have no competing interests.